The Astronomical Journal, 146:17 (10pp), 2013 July doi:10.1088/0004-6256/146/1/17

THE PECULIAR PHOTOMETRIC PROPERTIES OF 2010 WG9: A SLOWLY ROTATING TRANS-NEPTUNIAN OBJECT FROM THE OORT CLOUD

David Rabinowitz[1], Megan E. Schwamb[1], Elena Hadjiyska[1], Suzanne Tourtellotte[2], and Patricio Rojo[3]
[1] Center for Astronomy and Astrophysics, Yale University, New Haven, CT, USA
[2] Astronomy Department, Yale University, New Haven, CT, USA
[3] Department of Astronomy, University of Chile, Santiago, Chile
Received 2013 April 12; accepted 2013 May 20; published 2013 June 14

ABSTRACT

We present long-term *BVRI* observations of 2010 WG9, an ∼100 km diameter trans-Neptunian object (TNO) with an extremely high inclination of 70° discovered by the La Silla–QUEST southern sky survey. Most of the observations were obtained with ANDICAM on the SMARTS 1.3 m at Cerro Tololo, Chile from 2010 December to 2012 November. Additional observations were made with EFOSC2 on the 3.5 m NTT telescope of the European Southern Observatory at La Silla, Chile in 2011 February. The observations reveal a sinusoidal light curve with amplitude 0.14 mag and period 5.4955 ± 0.0025 days, which is likely half the true rotation period. Such long rotation periods have previously been observed only for tidally evolved binary TNOs, suggesting that 2010 WG9 may be such a system. We predict a nominal separation of at least 790 km, resolvable with the *Hubble Space Telescope* and ground-based systems. We measure $B - R = 1.318 \pm 0.029$ and $V - R = 0.520 \pm 0.018$, consistent with the colors of modestly red Centaurs and Damocloids. At *I*-band wavelengths, we observe an unusually large variation of color with rotational phase, with $R - I$ ranging from 0.394 ± 0.025 to 0.571 ± 0.044. We also measure an absolute *R*-band absolute magnitude of 7.93 ± 0.05 and solar phase coefficient of 0.049 ± 0.019 mag deg^{-1}.

Key words: Kuiper Belt: general – Kuiper Belt objects: individual (2010 WG9) – Oort Cloud

Online-only material: color figures

1. INTRODUCTION

Here we present photometric observations of 2010 WG9, a trans-Neptunian object (TNO) with an unusually high inclination discovered by the La Silla–QUEST southern-sky survey for TNOs (Rabinowitz et al. 2012). With perihelion $q = 18.8$ AU, aphelion $Q = 88.3$ AU, and inclination $i = 70\overset{\circ}{.}2$, 2010 WG9 is one of only five known solar system bodies with $i > 60°$ and $q > 15$ AU, including the retrograde object 2008 KV42 (Gladman et al. 2009). Brasser et al. (2012b) refer to these bodies as high-inclination, high-perihelion (HiHq) objects. Because they have dynamical lifetimes of ∼200 Myr limited by encounters with Neptune and Uranus, there must be a reservoir resupplying them. Brasser et al. show that the Oort Cloud is the most likely source. On gigayear timescales galactic tides can lower the perihelia of some Oort Cloud bodies to the point where they are captured by Uranus and/or Neptune and thereby removed from the Oort Cloud. Thus, some HiHq objects may derive from the same inner Oort-Cloud population revealed by Sedna and 2000 CR105 (Fernandez & Brunini 2000; Brasser et al. 2012a). The likelihood for the migration is extremely small ($\sim 10^{-5}$), explaining why HiHq bodies were not predicted in earlier numerical simulations (e.g., Levison et al. 2001). Nonetheless there are enough Oort Cloud bodies to supply the observed population. The alternative possibility, that HiHq bodies migrate from the Kuiper Belt through planetary interactions alone, is vanishingly small.

Observations of 2010 WG9 thus present a unique opportunity to measure the physical properties of a likely returning member of the Oort Cloud before it has reached the inner solar system. Unlike long-period and Halley-family comets, Damocloids, and other high-inclination objects with perihelia interior to Saturn's orbit, 2010 WG9 has likely never approached the Sun closer than Uranus since its ejection into the Oort Cloud early in the solar system's history. Furthermore, the body has likely spent most of the age of the solar system at distances larger than ∼1000 AU, where volatile loss rates due to solar heating are negligible. In the Kuiper Belt, on the other hand, it is expected that all but the largest bodies have lost their surface volatiles owing to solar heating (Schaller & Brown 2007). It is therefore possible that 2010 WG9 retains a pristine surface composition compared to most TNOs and to previously observed bodies of likely Oort-Cloud origin.

Here we present measurements of the brightness of 2010 WG9 in *B*, *V*, *R*, and *I* measured at several different epochs, and long-term *I*- and *R*-band observations revealing the rotation period, color, and slope of the solar phase curve. The resulting light curve reveals several physical properties rarely observed for outer solar system bodies, including an extremely slow rotation and large variations in color across the surface. To put the observed color in context, we compare the mean colors we observe for 2010 WG9 to other bodies on HiHq orbits and to other bodies that have likely migrated from the Oort Cloud into the inner solar system. We also compare to the Centaurs, which are generally representative of the Kuiper Belt. These comparisons probe the diversity of colors for Oort-Cloud bodies, previously constrained only by observations of the devolatilized cores of long-period comets and of the few known Sedna-like bodies. Our color comparisons also test for any differences between the HiHq bodies and the Kuiper Belt objects (KBOs) which might result from differences in their regions of formation in the inner solar system. We also discuss the implications of the unusual rotation and color variability assuming 2010 WG9 is a tidally evolved binary.

2. OBSERVATIONS

2.1. *Instrumentation*

Most of the observations we report here were obtained in service mode by on-site operators at Cerro Tololo, Chile using the optical channel of the A Novel Dual Imaging Camera

Table 1
Observing Circumstances

Telescope	Instrument	Filters	Dates	No. Nights	Mode	Conditions
SMARTS 1.3 m	ANDICAM	B, V, I, R	2010 Dec 3, 4	2	Service	Photometric
SMARTS 1.3 m	ANDICAM	R	2010 Dec 22–2011 Mar 26	44	Service	Mixed
NTT 3.5 m	EFOSC2	B, V, R, i	2011 Feb 5, 6	2	Classical	Photometric
NTT 3.5 m	EFOSC2	B, R	2011 Feb 8	1	Classical	Cirrus
SMARTS 1.3 m	ANDICAM	I, R	2012 Nov 10–20	11	Service	Mixed

(ANDICAM) on the Small and Moderate Aperture Research Telescope System (SMARTS) 1.3 m telescope. The optical imager is a Fairchild 2K × 2K CCD with a pixel scale of 0$''$.37. Table 1 summarizes the observing circumstances in each of three observing runs. All of the SMARTS observations consist of single 10 minute exposures in Johnson/Cousins B, V, R, and I. Observations made 2010 December 3 and 4 were taken in photometric conditions. Additional pairs of R-band images were taken nearly every other night from 2010 December 22 to 2011 March 26 in mixed conditions. Finally, pairs of both R- and I-band data were taken every night from 2012 November 10 to 20, also in mixed conditions. Seeing typically ranged from 1$''$.0 to 2$''$.0. All images were pre-processed using standard bias and twilight flat fields.

For more precise photometry, we made observations in classical mode with the 3.5 m New Technology Telescope (NTT) at the European Southern Observatory (ESO) at La Silla, Chile using the ESO Faint Object Spectrograph and Camera (EFOSC2). The imaging array consists of a thinned, 2K × 2K Loral/Lesser CCD with 15 μm pixels. Exposures were taken 2 × 2 binned, yielding a pixel scale of 0$''$.24. We recorded exposures in Bessel B, V, and R and Gunn i in photometric conditions on 2011 February 5 and 6, with seeing of 0$''$.6–0$''$.8 on February 5 and 1$''$.1–1$''$.3 on February 6. We recorded additional R- and B-band observations spanning 2.6 hr on 2011 February 8 in non-photometric conditions (thin cirrus) with seeing ranging from 0$''$.9 to 1$''$.3. Target exposure times on all three nights ranged from 60 to 600 s. All observations were pre-processed using bias fields and twilight flats. Note that on February 8, R-band observations of the same target field were made in service mode with the SMARTS 1.3 m at Cerro Tololo, where the conditions were photometric.

2.2. SMARTS Calibrations

We calibrated all of the SMARTS data we obtained prior to 2012 using our standard reduction procedure described in detail by Rabinowitz et al. (2006, 2007). In this method, we first choose bright field stars present in all the target images observed on photometric nights and calibrate them with respect to Landolt standards. We then calibrate the target in each exposure (including observations on non-photometric nights) by measuring the target flux relative to the calibrated field stars in the same image. To optimize signal to noise, we use a small aperture for these relative flux measurements (diameter 2$''$.2, slightly larger than the typical seeing). We use the APHOT routines in IRAF to make these measurements. Our typical systematic error using this method is ∼1.5%.

We used a new method to calibrate the 2012 SMARTS data. Instead of calibrating secondary standards in each field, which would have required additional observations on photometric nights, we used the UCAC4 catalog (Zacharias et al. 2013) to identify stars with known magnitudes in Johnson B and V and Gunn g, r, and i in each target field. Note that the UCAC4 catalog has incorporated the results of the recently completed AAVSO Photometric All-Sky Survey (Henden et al. 2012), which has covered nearly the whole sky in $BVgri$ down to mag $V \sim 16$. We found that all of our 2012 SMARTS exposures contain at least three UCAC4 stars with magnitudes faint enough to be unsaturated in our 10 min exposures, yet bright enough to have precisely measured magnitudes. For these calibrations we use SExtractor to determine target and field star magnitudes (using a small aperture of 2$''$.2 diameter) rather than relying on IRAF routines. We also convert the cataloged Gunn g, r, and i values listed by UCAC4 to Johnson R and I using the following conversion formulae known to be accurate to ∼1% for most stars (see http://www.sdss.org/dr5/algorithms/sdssUBVRITransform.html):

$$R = r - 0.1837 * (g - r) - 0.0971$$

$$I = r - 1.2444 * (r - i) - 0.3820.$$

For most of the 2012 SMARTS fields, we find that the above procedure yields zero-point calibrations with precision better than 5%.

2.3. NTT Calibrations

To calibrate our photometric NTT observations (2011 February 5 and 6), we used standard regression methods to determine the difference between cataloged and instrumental magnitudes of observed Landolt standards in each bandpass as a linear function of air mass and source color. From multiple observations of many different standards at widely varying air mass, we derived solutions yielding observed minus predicted magnitudes with variance of 1.4%–2.7% on February 5 and 1.0%–1.2% on February 6. We then measured the flux of our target within small apertures (diameters 0$''$.72 and 1$''$.2 on February 5 and 6, respectively), adjusted these fluxes using an aperture correction determined separately for each image from the field stars, and used our calibration to determine the resulting magnitudes in each filter.

To analyze our non-photometric NTT observations (2011 February 8), all of which were exposures of the same field over a time span of 0.11 days, we reprocessed the images to optimize the precision for relative photometry. The purpose was to remove the signal from very faint stars and galaxies near the moving location of the target. Although no such sources are obvious in the images, their presence at a faint level comparable to the noise in the sky background limits our photometric precision. The reprocessing procedure, performed separately for the B- and R-band images, was as follows.

1. We registered the images with respect to the field stars (linear pixel shifts) and scaled the images to have unity value for the mean sky background. This transformed

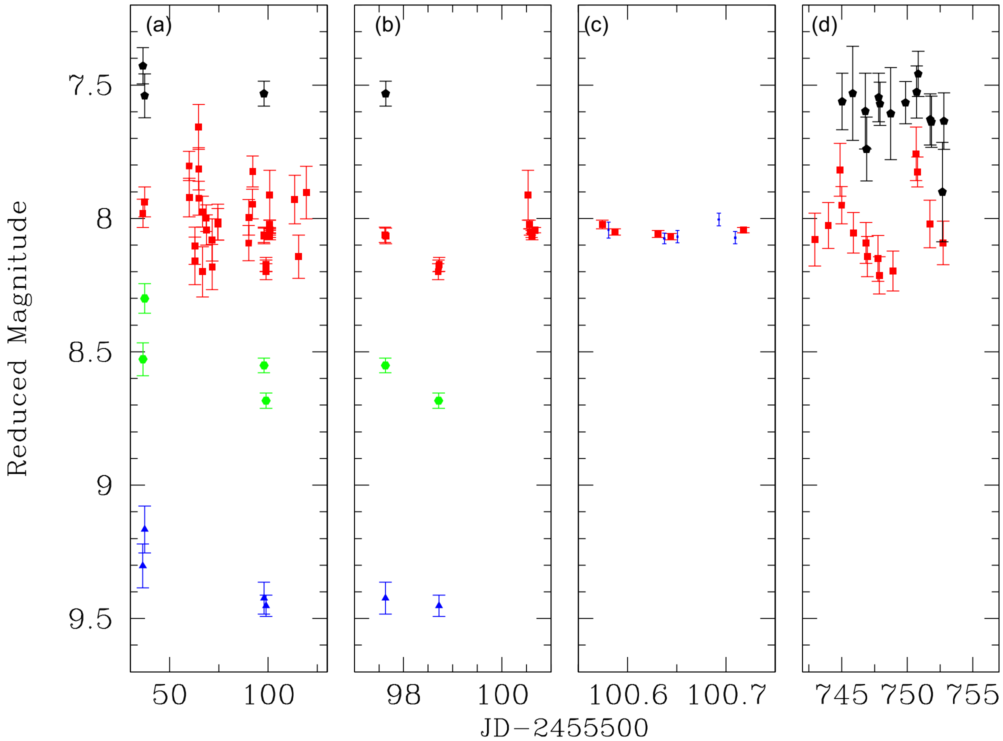

Figure 1. Reduced B, V, R, I magnitudes vs. Julian Date for 2010 WG9 at four different epochs: (a) SMARTS observations from 2010 and 2011; (b) NTT observations from 2011 February 5, 6, and 8; (c) NTT observations from 2011 February 8; (d) SMARTS observations from 2012 November 10–20. Each bandpass is represented by a different symbol: blue triangles (B), green hexagons (V), red squares (R), and black pentagons (I). In panel (c), small blue points represent B-band data that has been relatively calibrated, and then offset to best overlap the R-band data. These data are excluded from the analysis in the text, except where specifically cited.

(A color version of this figure is available in the online journal.)

our initial set of bias- and flat-field-corrected images to a normalized set.

2. We median-averaged the normalized images to obtain a single, deep exposure of the field in each pass-band. Because the target moved 16″.5 over the time span of the image set, the target signal was removed by the median averaging.
3. We divided each normalized image by the median image to obtain a set of sky-divided images from which the signal from the sky, field stars, and galaxies was largely removed. The only signal remaining in each image was that of the target.
4. For each target observation, we used a fixed small aperture (1″.9 diameter, comparable to the seeing) to measure the target magnitude in the sky-divided image, and also to measure the average magnitude of a fixed set of field stars in the normalized image. Any variations in the target signal resulting from changes in the PSF or sky transparency would affect the brightness of the target and field stars equally.
5. We subtracted the average field-star magnitude from the target magnitudes to obtain a relatively calibrated light curve.

After using the above procedure to obtain a relative calibration, we were able to absolutely calibrate the R-band observations with respect to secondary standards in the field. We were able to calibrate these field standards using our SMARTS observations of the same field that had been incidentally taken the same night in photometric conditions. Unfortunately, we could not calibrate the B-band magnitudes of the field stars because we did not obtain a photometric B-band observation of the field. Hence the resulting B-band magnitudes, while precisely calibrated relative to one another, cannot be referred to an absolute scale. To make the observations useful for measuring rotational variability in the R band, we have added a zero point so that their mean value matches the mean for the R-band observations observed the same night (see discussion of Figure 4 in Section 3.1).

Table 2 lists the resulting brightness measurements (M') and their measurement error (σ) from all of our SMARTS and NTT observations, excluding target measurements contaminated by cosmic ray hits or nearby bright stars. We also exclude R-band observations with $\sigma > 0.1$ mag. Table 2 also lists the Julian Date (JD) at the mid-time of each exposure (t), the solar phase angle (α), the target distance to the Sun (r_s) and to the Earth (r_e), the reduced magnitude ($M = M' - 5\log[r_s\ r_e]$), and the light travel time (Δt) relative to the first observation in the table. In the proceeding analysis of the light curve, all observation times have been adjusted by Δt to account for the relative motion of the target and Earth over the long time span of the observations. The largest time correction is ∼10 minutes. The B-band NTT observations from 2011 February 8, adjusted to align with the R-band light curve, appear in Table 2 with label "R_B."

3. RESULTS AND ANALYSIS

3.1. The Rotational Light Curve

Figures 1(a)–(d) show our measured values of the reduced magnitude in the B, V, R, and I bands versus JD. In the absence of rotational modulation and solar phase dependence, each of these light curves would be time dependent. The plot is separated into four panels to highlight the observations corresponding

Table 2
Photometric Observations of 2010 WG9

JD-2450000	Δt (minutes)	M' (mag)	σ (mag)	M (mag)	α (°)	r_s (AU)	r_e (AU)	Filter	Telescope
5534.65033	0.00	22.131	0.082	9.303	1.843	19.567	18.798	*B*	SMARTS-1.3
5534.65793	0.00	21.356	0.062	8.528	1.843	19.567	18.798	*V*	SMARTS-1.3
5534.66553	0.00	20.809	0.053	7.981	1.843	19.567	18.798	*R*	SMARTS-1.3
5534.67316	0.00	20.256	0.068	7.428	1.843	19.567	18.798	*I*	SMARTS-1.3
5535.60153	0.00	21.994	0.088	9.166	1.839	19.568	18.798	*B*	SMARTS-1.3
5535.60912	0.00	21.128	0.055	8.300	1.839	19.568	18.798	*V*	SMARTS-1.3
5535.61672	0.00	20.766	0.056	7.938	1.839	19.568	18.798	*R*	SMARTS-1.3
5535.62435	0.00	20.368	0.082	7.540	1.838	19.568	18.798	*I*	SMARTS-1.3
5553.66254	0.34	20.654	0.137	7.819	1.914	19.584	18.839	*R*	SMARTS-1.3
5553.71019	0.34	20.931	0.187	8.096	1.915	19.584	18.840	*R*	SMARTS-1.3
5558.67902	0.55	20.641	0.055	7.803	1.982	19.589	18.865	*R*	SMARTS-1.3
5558.73460	0.56	20.760	0.072	7.922	1.983	19.589	18.865	*R*	SMARTS-1.3
5561.63859	0.70	20.943	0.070	8.102	2.028	19.591	18.883	*R*	SMARTS-1.3
5561.67750	0.71	21.000	0.089	8.159	2.029	19.591	18.883	*R*	SMARTS-1.3
5563.65215	0.81	20.499	0.084	7.657	2.062	19.593	18.896	*R*	SMARTS-1.3
5563.66033	0.81	20.656	0.079	7.814	2.062	19.593	18.896	*R*	SMARTS-1.3
5563.69481	0.82	20.766	0.064	7.924	2.063	19.593	18.896	*R*	SMARTS-1.3
5565.64137	0.93	20.819	0.058	7.975	2.097	19.595	18.910	*R*	SMARTS-1.3
5565.69402	0.93	21.044	0.094	8.200	2.098	19.595	18.911	*R*	SMARTS-1.3
5567.64210	1.06	20.845	0.050	7.999	2.134	19.597	18.925	*R*	SMARTS-1.3
5567.70360	1.06	20.889	0.057	8.043	2.135	19.597	18.926	*R*	SMARTS-1.3
5570.59325	1.25	21.031	0.085	8.182	2.190	19.599	18.949	*R*	SMARTS-1.3
5570.68273	1.26	20.930	0.079	8.081	2.191	19.599	18.950	*R*	SMARTS-1.3
5573.58771	1.47	20.866	0.067	8.014	2.247	19.602	18.975	*R*	SMARTS-1.3
5573.63733	1.47	20.874	0.059	8.022	2.248	19.602	18.975	*R*	SMARTS-1.3
5577.67127	1.79	21.002	0.147	8.145	2.327	19.606	19.013	*R*	SMARTS-1.3
5577.70409	1.79	20.932	0.135	8.075	2.327	19.606	19.014	*R*	SMARTS-1.3
5581.60208	2.12	20.910	0.154	8.048	2.403	19.609	19.053	*R*	SMARTS-1.3
5581.65115	2.13	20.831	0.161	7.969	2.404	19.610	19.054	*R*	SMARTS-1.3
5589.60134	2.87	20.965	0.066	8.092	2.549	19.617	19.143	*R*	SMARTS-1.3
5589.65287	2.87	20.869	0.067	7.996	2.550	19.617	19.144	*R*	SMARTS-1.3
5591.61610	3.07	20.822	0.056	7.946	2.584	19.619	19.167	*R*	SMARTS-1.3
5591.66986	3.07	20.700	0.058	7.824	2.585	19.619	19.168	*R*	SMARTS-1.3
5597.56353	3.69	20.946	0.029	8.061	2.677	19.624	19.242	*R*	NTT-3.5
5597.57321	3.69	21.436	0.027	8.551	2.677	19.624	19.242	*V*	NTT-3.5
5597.57670	3.69	22.309	0.060	9.424	2.677	19.624	19.242	*B*	NTT-3.5
5597.58002	3.69	20.417	0.047	7.532	2.677	19.624	19.242	*I*	NTT-3.5
5597.58354	3.69	20.951	0.029	8.066	2.677	19.624	19.242	*R*	NTT-3.5
5598.67190	3.81	21.087	0.030	8.200	2.693	19.625	19.256	*R*	NTT-3.5
5598.67706	3.81	21.065	0.022	8.178	2.693	19.625	19.256	*R*	NTT-3.5
5598.68125	3.81	21.570	0.029	8.683s	2.693	19.625	19.256	*V*	NTT-3.5
5598.68648	3.81	22.339	0.040	9.452	2.693	19.625	19.256	*B*	NTT-3.5
5598.69171	3.81	21.059	0.026	8.172	2.693	19.625	19.256	*R*	NTT-3.5
5600.53825	4.01	20.803	0.094	7.913	2.718	19.627	19.281	*R*	SMARTS-1.3
5600.56864	4.02	20.854	0.015	7.964	2.719	19.627	19.281	*R*	NTT-3.5
5600.57085	4.02	20.934	0.030	8.044	2.719	19.627	19.281	R_B	NTT-3.5
5600.57864	4.02	20.888	0.012	7.998	2.719	19.627	19.281	*R*	NTT-3.5
5600.61215	4.02	20.896	0.012	8.006	2.719	19.627	19.282	*R*	NTT-3.5
5600.61438	4.02	20.965	0.020	8.075	2.719	19.627	19.282	R_B	NTT-3.5
5600.62217	4.02	20.884	0.012	7.994	2.719	19.627	19.282	*R*	NTT-3.5
5600.62439	4.02	20.958	0.023	8.068	2.719	19.627	19.282	R_B	NTT-3.5
5600.65358	4.03	20.908	0.012	8.018	2.720	19.627	19.282	*R*	NTT-3.5
5600.65707	4.03	20.894	0.024	8.004	2.720	19.627	19.282	R_B	NTT-3.5
5600.66963	4.03	20.962	0.023	8.072	2.720	19.627	19.283	R_B	NTT-3.5
5600.67871	4.03	20.891	0.011	8.001	2.720	19.627	19.283	*R*	NTT-3.5
5612.60374	5.40	20.711	0.147	7.801	2.843	19.638	19.448	*R*	SMARTS-1.3
5612.64708	5.41	20.830	0.194	7.920	2.843	19.638	19.449	*R*	SMARTS-1.3
5613.55909	5.52	20.841	0.091	7.929	2.850	19.639	19.462	*R*	SMARTS-1.3
5613.65420	5.53	20.739	0.167	7.827	2.850	19.639	19.463	*R*	SMARTS-1.3
5615.55986	5.76	21.058	0.081	8.143	2.862	19.641	19.491	*R*	SMARTS-1.3
5615.62756	5.77	20.802	0.105	7.887	2.863	19.641	19.492	*R*	SMARTS-1.3
5619.52076	6.24	20.825	0.099	7.903	2.881	19.645	19.548	*R*	SMARTS-1.3
5631.57383	7.72	20.811	0.150	7.868	2.883	19.656	19.726	*R*	SMARTS-1.3
5633.52340	7.96	21.180	0.128	8.234	2.876	19.658	19.755	*R*	SMARTS-1.3
5633.58313	7.96	21.058	0.167	8.112	2.875	19.658	19.756	*R*	SMARTS-1.3

Table 2
(Continued)

JD-2450000	Δt (minutes)	M' (mag)	σ (mag)	M (mag)	α (°)	r_s (AU)	r_e (AU)	Filter	Telescope
5635.51741	8.20	20.644	0.146	7.695	2.866	19.660	19.784	*R*	SMARTS-1.3
5635.58073	8.21	21.260	0.271	8.310	2.866	19.660	19.785	*R*	SMARTS-1.3
5639.50821	8.68	20.818	0.205	7.862	2.841	19.663	19.842	*R*	SMARTS-1.3
5639.57567	8.69	20.785	0.240	7.829	2.840	19.663	19.843	*R*	SMARTS-1.3
5645.51194	9.40	20.991	0.118	8.025	2.787	19.669	19.928	*R*	SMARTS-1.3
5645.55864	9.40	20.888	0.108	7.922	2.787	19.669	19.929	*R*	SMARTS-1.3
5647.50265	9.63	20.924	0.101	7.955	2.766	19.671	19.956	*R*	SMARTS-1.3
5647.54855	9.63	21.108	0.143	8.138	2.765	19.671	19.957	*R*	SMARTS-1.3
6242.70228	6.55	21.078	0.099	8.079	1.931	20.315	19.587	*R*	SMARTS-1.3
6243.64725	6.49	21.194	0.142	8.196	1.906	20.316	19.581	*R*	SMARTS-1.3
6243.75179	6.49	21.024	0.086	8.026	1.903	20.316	19.580	*R*	SMARTS-1.3
6244.67056	6.44	20.816	0.099	7.818	1.879	20.317	19.574	*R*	SMARTS-1.3
6244.78920	6.43	20.948	0.070	7.950	1.876	20.318	19.573	*R*	SMARTS-1.3
6244.83244	6.43	20.560	0.106	7.562	1.875	20.318	19.573	*I*	SMARTS-1.3
6245.65362	6.38	20.528	0.176	7.531	1.854	20.319	19.568	*I*	SMARTS-1.3
6245.70401	6.38	21.051	0.076	8.054	1.853	20.319	19.568	*R*	SMARTS-1.3
6246.64226	6.33	20.595	0.142	7.598	1.828	20.320	19.562	*I*	SMARTS-1.3
6246.68500	6.33	21.089	0.077	8.092	1.827	20.320	19.561	*R*	SMARTS-1.3
6246.73468	6.33	20.737	0.120	7.740	1.826	20.320	19.561	*I*	SMARTS-1.3
6246.79584	6.33	21.140	0.075	8.143	1.824	20.320	19.561	*R*	SMARTS-1.3
6247.61837	6.28	21.146	0.086	8.150	1.803	20.321	19.556	*R*	SMARTS-1.3
6247.67519	6.28	20.542	0.091	7.546	1.802	20.321	19.556	*I*	SMARTS-1.3
6247.72594	6.28	21.209	0.070	8.213	1.800	20.321	19.555	*R*	SMARTS-1.3
6247.78166	6.28	20.566	0.081	7.570	1.799	20.321	19.555	*I*	SMARTS-1.3
6248.61765	6.24	20.603	0.173	7.607	1.778	20.322	19.550	*I*	SMARTS-1.3
6248.66425	6.24	21.042	0.130	8.046	1.777	20.322	19.550	*R*	SMARTS-1.3
6248.78505	6.23	21.193	0.075	8.197	1.774	20.322	19.549	*R*	SMARTS-1.3
6249.76990	6.18	20.561	0.079	7.566	1.749	20.324	19.544	*I*	SMARTS-1.3
6250.59534	6.15	20.753	0.100	7.758	1.728	20.325	19.540	*R*	SMARTS-1.3
6250.64179	6.15	20.521	0.098	7.526	1.727	20.325	19.539	*I*	SMARTS-1.3
6250.69644	6.14	20.821	0.056	7.826	1.726	20.325	19.539	*R*	SMARTS-1.3
6250.75914	6.14	20.453	0.085	7.458	1.724	20.325	19.539	*I*	SMARTS-1.3
6251.65839	6.10	21.015	0.089	8.021	1.702	20.326	19.534	*R*	SMARTS-1.3
6251.69284	6.10	20.623	0.096	7.629	1.702	20.326	19.534	*I*	SMARTS-1.3
6251.78558	6.10	20.632	0.096	7.638	1.699	20.326	19.534	*I*	SMARTS-1.3
6252.59496	6.07	21.300	0.252	8.306	1.680	20.327	19.530	*R*	SMARTS-1.3
6252.64225	6.07	20.895	0.186	7.901	1.679	20.327	19.530	*I*	SMARTS-1.3
6252.70388	6.06	21.086	0.082	8.092	1.677	20.327	19.529	*R*	SMARTS-1.3
6252.76114	6.06	20.629	0.106	7.635	1.676	20.327	19.529	*I*	SMARTS-1.3

to the different observing campaigns listed in Table 2. Note that the time span is very different for each panel. Panel (a) shows only the SMARTS results obtained in 2010 and 2011 (time span 100 days). Panel (b) shows all of the NTT results (time span 4 days) and the single *R*-band observation obtained concurrently using SMARTS on 2011 February 8. Panel (c) shows an expanded view of the NTT observations obtained 2011 February 8 alone (the relatively calibrated *B*-band observations, shifted to overlay the *R*-band observations, are shown as small points in blue). Panel (d) shows the SMARTS observations obtained on 2012 November 10–20. Note that we exclude the *B*-band observations obtained on 2011 February 8 from the analysis presented below, except where specifically cited.

Figures 1(a)–(d) show that the observations have significant scatter with peak-to-peak amplitude ~0.3 mag. For each bandpass, Table 3 shows the number of observations, N, and the residual χ^2 for the distribution (see column labeled "${\chi_0}^2$"). Specifically, we evaluate the following expression:

$$\chi_0^2 = \sum_{\rm i} [M_{\rm i} - \langle M \rangle]^2 / \sigma_{\rm i}^2. \tag{1}$$

Table 3
χ^2 for Measured Light Curves

Bandpass	N	${\chi_0}^2$	${\chi_L}^2$	${\chi_S}^2$
B	4	10.3	3.5	1.1
V	4	40.2	3.6	5.3
R	49	232.7	64.5	91.3
I	17	13.2	21.0	33.2
$R_{\rm NTT}$	10	12.5	14.7	34.9

The sum is over all observations, $i = 1$–N, with magnitude, $M_{\rm i}$, measurement error, $\sigma_{\rm i,}$ and where $\langle M \rangle$ is the weighted average magnitude,

$$\langle M \rangle = \sum_{\rm i} [M_{\rm i}/\sigma_{\rm i}^2] \Big/ \sum_{\rm i} [1/\sigma_{\rm i}^2]. \tag{2}$$

The resulting χ^2 values are much larger than the number of degrees of freedom, $N-1$. This is particularly evident for the *R*-band observations, where $\chi^2 = 232$ with $N = 49$. This indicates significantly more variation than would be expected by chance for a source with no intrinsic variability. The scatter appears only when comparing observations taken days apart (Figures 1(a), (b), and (d)), but not over an interval of a few hours (Figure 1(c)). The likely cause of the variation is rotational modulation with a period of at least a few days.

There is also a long-term α-dependence to the observations. Fitting a linear relation between the R-band magnitude and α (which varies from 1°.7 to 2°.9) we measure a slope $\beta = 0.053 \pm 0.020$ mag deg^{-1}. This variation is significant, but cannot explain the day-to-day variations we observe. Subtracting the solar phase dependence reduces the R-band χ^2 from 232 to 212, but this is still significantly larger than the number of degrees of freedom ($N-2 = 47$). In Section 3.2 we re-derive β after fitting and subtracting rotational variability. This changes the result slightly, but not significantly. For the purposes of measuring variability, we adopt the above value as it simplifies the analysis.

To search for a periodicity, we first removed the measured phase-angle dependence from the R-band observations plotted in Figures 1(a)–(d). To the resulting light curve we then fit a sinusoidal function of time, $F(t)$, with amplitude, A, and period, P, given by

$$F(t) = A\sin(2\pi[\phi + \omega(P, t)]), \tag{3}$$

where $\omega(P, t)$ is the rotational phase, $\omega(P, t) = (t - t_o)/P$ at time t with respect to chosen epoch t_o, and ϕ is a rotational phase offset. To obtain the best fit values for parameters P, A, and ϕ, we then iteratively minimized χ^2 given by

$$\chi^2 = \sum_i [M_i - \langle M\rangle - F(t_i)]^2 / \sigma_i^2. \tag{4}$$

The minimum value was found by varying A from 0.1 to 0.2 mag by increments of 0.01 mag, varying ϕ over its full range, 0–1, by increments of 0.01, and varying P from 0.05 to 20 days in uniform logarithmic increments, $\log[20.0/0.05]/10^5$. This search range for A comfortably brackets the amplitudes we would expect given the scatter in the observations. The search range for P covers the minimum period expected for a strengthless rubble pile ($\sim$0.08 days) up to the maximum capable of producing the day-to-day variations we observe ($\sim$10 days). Epoch t_o was fixed at JD = 2455500.

Figure 2 shows the resulting plot of χ^2 versus P, where χ^2 is the minimum value found for all values of A and ϕ. It is apparent that there is one conspicuous minimum, $P_L = 5.4955$ days, where $\chi^2 = 64.4$. Given the large reduction in χ^2 compared to ${\chi_0}^2$, it is clear that there are significant correlations in the R-band light curve with this period. We obtain the best fit with $A = 0.144$ mag and $\phi = 1.27$. Fixing A at this best value, we then estimate an uncertainty of ± 0.0025 days for P by finding the range of periods centered on P_L such that the minimum χ^2 (for all values of ϕ) exceeds $\chi^2 = 64.4$ by less than 2.3. This yields the 1σ uncertainty when two degrees of freedom (ϕ and P) are allowed to vary.

There is another χ^2 minimum at $P_S = 1.2226 \pm 0.0001$ days, where $\chi^2 = 91.8$ (with $A = 0.130$ mag and $\phi = 4.30$). Given the much larger χ^2 for this secondary minimum compared to P_L, it is clear that a sinusoid with this period does not fit the data as well. Also, one of these periods is clearly an alias of the other because $P_L/P_S = 4.504$ is very close to a small integer ratio, 9/2. The ambiguity results from the one- and two-day sampling intervals of the SMARTS observations in 2010 and 2011, which make up the bulk of the R-band observations. It is likely that P_L is the correct period and P_S is the alias. However, in both cases the χ^2 value is significantly larger than would be expected by chance given the number of degrees of freedom (46) in the sinusoidal fit (the likelihood is less than 5% for $\chi^2 > 62$). This implies that the measurement errors are larger than we have estimated, or that a simple sinusoid is not the best fit to the light curve. For example, adding a 3% systematic error in quadrature to each of our SMARTS R-band observations lowers the best-fit χ^2 to 56, which has a chance likelihood of 15%. Below we give consideration to both period solutions and provide a detailed comparison of the model light curves to the observations in order to decide the correct value.

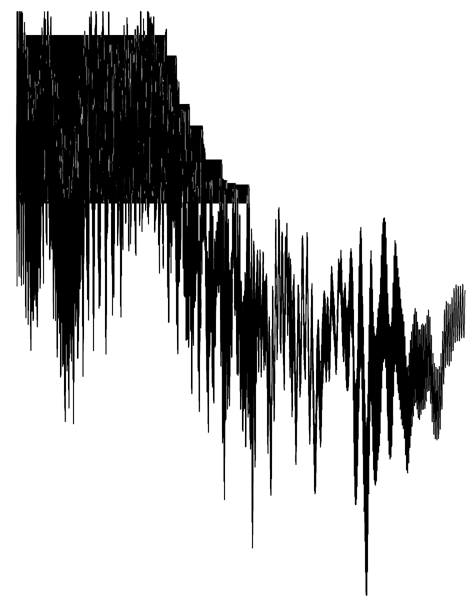

Figure 2. Periodogram showing χ^2 vs. period for sinusoidal fits to the data. The best fit periods are found at $P_L = 5.4955$ days and $P_S = 1.2226$ days. A detailed analysis shows that P_L is the correct period.

Figures 3(a) and (b) show the phased rotational light curves we obtain in B, V, R, and I when we assume $P = P_L$ and P_S, respectively. Each curve in each figure is a plot of the same data we show in Figure 1, but with JD replaced by the fractional part of the rotational phase, ω_i. The light curves are repeated over two periods to show continuity. Also, all the observations have been adjusted to remove the measured R-band α dependence, as discussed above. For each period, the best-fit R-band sinusoid, $F(t)$, is plotted as a solid line. For comparison with each of the other bandpasses, $F(t)$ is re-plotted with an offset matching the measured values for $B-R$, $V-R$, and $I-R$ (see below). Table 3 lists the χ^2 values we obtain for each light curve after subtracting $F(t)$ (see columns labeled "${\chi_L}^2$" and "${\chi_S}^2$"). These were computed using Equations (1) and (2), but with M_i replaced by $M_i - F(t_i)$.

Comparing Figures 3(a) and (b), it is not obvious by visual inspection which period yields the best fit. In both cases, $F(t)$ faithfully follows the phased R-band oscillations, and the B and V light curves are also well fit. This fitting of the B and V observations by an R-band light curve shows that the observed oscillations are true rotational modulations rather than

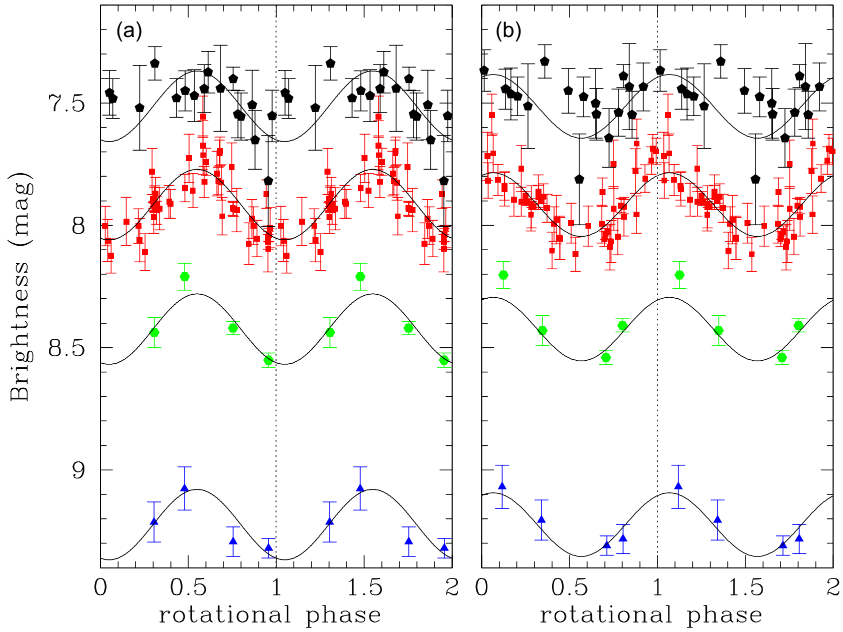

Figure 3. Rotationally phased light curves in B, V, R, and I for two different periods: (a) $P_{\mathrm{L}} = 5.4955$ days and (b) $P_{\mathrm{S}} = 1.2226$ days. Each bandpass is represented by a different symbol, as explained in Figure 1. All light curves are repeated over two phase cycles to illustrate continuity across cycle boundaries. In each panel, the black curves are the best sinusoidal fit to the R-band data for the respective period. To match the B, V, and I bandpasses, the R-band fit has been offset by the measured colors $B-V$, $V-R$, and $I-R$. Both periods appear to fit the B, V, and R measurements. Neither period provides a good fit to the I-band observations.

(A color version of this figure is available in the online journal.)

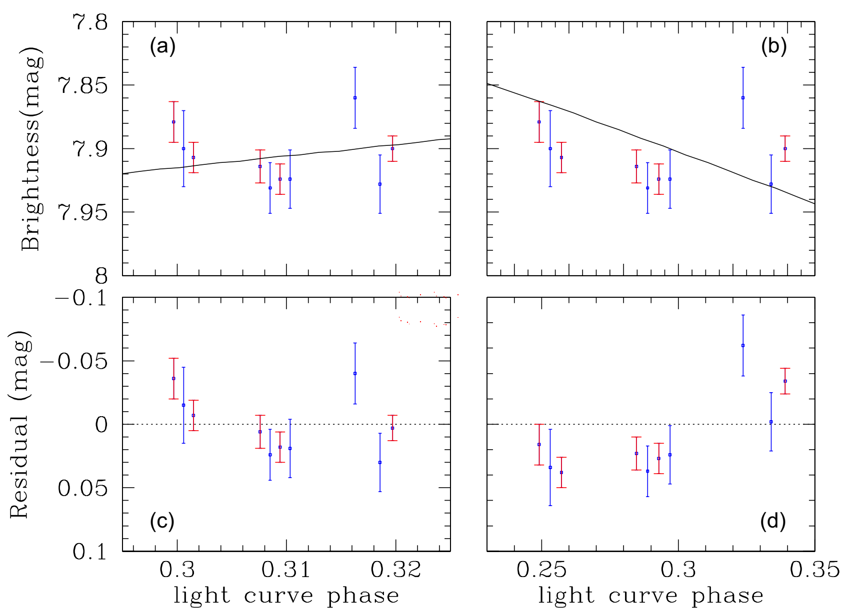

Figure 4. Rotationally phased light curves showing only the R- and B-band NTT observations from 2012 February 8. As in Figure 3, the black curves show the best sinusoidal fits. Panels (a) and (b) are for periods P_{L} and P_{S}, respectively. Panels (c) and (d) show the residuals after subtracting the fits in panels (a) and (b), respectively. The spread in residual is smallest for period P_{L}.

(A color version of this figure is available in the online journal.)

measurement artifacts. The χ^2 values listed in Table 3 for the B and V light curves are significantly reduced after subtracting $F(t)$ for both period solutions. The new values are now comparable to the number of degrees of freedom ($N-1 = 3$, for both bands), again validating the R-band fits. For neither period does $F(t)$ correlate well with the I-band light curve. After subtracting $F(t)$, the I-band variance increases, resulting in a larger χ^2. Thus it appears that the I-band rotational light curve differs from the light curve at bluer wavelengths, an indication of possible variations of color with rotational phase.

Figures 4(a) and (b) offer a more decisive comparison of the two period solutions. These figures again show the phased R-band data (red points) from Figures 3(a) and (b), respectively, but now restricted to the NTT measurements obtained on 2011 February 8 which span 2.6 hr and achieve the highest precision. The best-fit sinusoids from Figures 3(a) and (b) are again plotted as solid lines. We also show the B-band observations (small blue points), adjusted so that their mean matches the R-band mean over this restricted phase range. Although this sequence covers only a small range in rotation phase, it was fortuitously recorded at the mid-range of the light curve where rotational brightness variations are most rapid. Note that for P_L we expect a brightness slowly increasing with phase, whereas for P_S we expect an intensity diminishing with phase at a relatively rapid rate. The residuals after subtracting the fits are plotted in Figures 4(c) and (d), respectively.

Comparing Figures 4(a) and (b), it is now clear that P_L provides a much better fit than P_S. Though the R-band observations alone or in combination with the B band are consistent with the slow rise in brightness expected from P_L, they do not support the rapidly diminishing brightness expected for P_S. The χ^2 after subtracting $F(t)$ is 12.5 for P_L, with $N-1 = 9$ degrees of freedom. This scatter is only slightly larger than expected given the measurement errors, with a formal likelihood of $\sim$20% that the observations are consistent with $F(t)$. For P_S, on the other hand, we have $\chi^2 = 40$ which has vanishing likelihood (<0.01%). Hence we consider P_L to be the only valid period fitting the observations.

Our observations are not precise enough to determine if the number of peaks in the light curve is one per rotation, as expected from a single albedo spot on a spherical body, or two, as expected from the variation in the projected area of an elongated body. Bodies of $\sim$100 km diameter such as 2010 WG9 generally have rotational light curves with higher-amplitude oscillations than larger bodies (Sheppard et al. 2008; Benecchi & Sheppard 2013). This is indicative of greater asphericity for the smaller bodies, possibly due to past collisional impacts. It is therefore likely that the variability we see for 2010 WG9 is mostly from changes in the projected area, and the true rotation period is twice what we have measured, or 10.991 days.

3.2. Colors and Solar Phase Coefficient

Having found a good fit to the rotational light curve, we can now derive a rotation-corrected value for β and for the absolute magnitude, H_R, in the R band. We do this by linear regression, adjusting H and β to minimize χ^2 given by

$$\chi^2 = \sum_i [M_i - F(t_i) - (H + \beta\alpha_i)]^2 / \sigma_i^2, \qquad (5)$$

where α_i is the solar phase angle at time t_i, and M_i is the reduced R-band magnitude. This yields $H_R = 7.93 \pm 0.05$ mag and $\beta = 0.049 \pm 0.019$ mag deg^{-1}, with $\chi^2 = 56.9$ and $N-2 = 47$ degrees of freedom. This new value for β does not differ significantly from the value we derive earlier without rotation correction. For deriving colors, however, we adopt this new value as it has a marginal influence on the results.

To accurately measure the colors for 2010 WG9, we must account for both the rotational variability of the light curve and the α dependence. Two complementary methods are available. The first is to separately determine the colors at each epoch where B, V, R, and I were all measured together over a short time interval compared to the variability. The results from these different epochs can then be averaged together to determine the mean colors. The second method is to correct the observations for their α dependence and then to subtract the R-band sinusoidal fit, $F(t)$. With respect to the R band, we thus obtain the weighted average color, ΔM, for each bandpass using

$$\Delta M = \sum_i [M_i - F(t_i) - \beta\alpha_i]^2 / \sigma_i^2. \qquad (6)$$

In principle, this second method is a more accurate measure because $F(t) + \beta\alpha$ is a better estimate for the R-band magnitude at any given epoch than the individual R-band observations. We find that both methods give consistent results and adopt the second because the results are more precise.

Table 4
Average Colors for 2010 WG9

Color	N	ΔM (mag)	Unc. (mag)	χ^2
$B-R$	4	1.318	0.029	3.57
$V-R$	4	0.520	0.018	3.86
$R-I_1$	4	0.571	0.044	0.51
$R-I_2$	13	0.394	0.025	7.93

Notes. $R-I$ is evaluated separately for rotational phase 0.0–0.4 and 0.4–1.0. See text for details.

Table 4 lists the resulting colors, along with the number of measurements, N, used to determine the average and the residual χ^2. Note that we list $R-I$ for two ranges in rotational phase, $R-I_1$ for 0.0–0.4 and $R-I_2$ for 0.4–1.0. Close inspection of Figure 3(a) shows that the correlation between the I and R light curves is significant in both ranges, but there is a shift in $R-I$ from one range to the other. The resulting χ^2 values for $B-R$, $V-R$, $R-I_1$, and $R-I_2$ are all comparable to $N-1$, indicating good measures of the mean.

It is possible that the value we measure for β may depend on wavelength. Using Equation (5) above to separately measure β for the B, V, and I bandpasses, we derive $\beta = 0.082 \pm 0.083$, 0.120 ± 0.057, and -0.014 ± 0.061 mag deg^{-1}, respectively. Given their large uncertainties, however, none of these β values differs significantly from the R-band value. Many more observations in B, R, and I would be required to demonstrate a significant wavelength dependence. If there were a strong wavelength dependence, however, it would alter our color measurements by $\lesssim$0.1 mag. For example using $\beta = 0.082$ mag deg^{-1} instead of $\beta = 0.049$ mag deg^{-1} decreases $B-R$ from 1.32 to 1.24 mag.

4. DISCUSSION

4.1. Color

To put the colors we measure for 2010 WG9 into context with similar solar system objects, we present in Figure 5 a plot of $R-I$ versus $V-R$ for 2010 WG9 and for other inactive bodies that have likely returned from the Oort Cloud. Medium-sized red diamonds represent two other HiHq TNOs (2008 KV42 and 2002XU9 from Sheppard 2010). Red triangles represent three distant bodies with exceptionally high aphelion or perihelion suspected to come from the inner Oort Cloud (Sedna, 2006 SQ372, and 2000 OO67 from Sheppard 2010). Black squares represent the relatively nearby Damocloids thought to be devolatilized cores of Halley-type comets (from Jewitt 2005). Small green points represent the colors for Centaur asteroids listed in the MBOSS catalog (Hainaut et al. 2012). Unlike the other bodies represented in the figure, the Centaurs likely migrated from the Kuiper Belt without passing through the Oort Cloud. Their distribution of colors generally matches the colors of KBOs. Note that we represent 2010 WG9 in Figure 5 by two different symbols (large unfilled and filled diamonds), corresponding to the two values we measure for $R-I$ (rotational phases 0.0–0.4 and 0.4–1.0, respectively).

An examination of Figure 5 shows that the colors we measure for 2010 WG9 do not distinguish it from Centaurs, Damocloids, or KBOs in general. The likely implication is that it has a similar

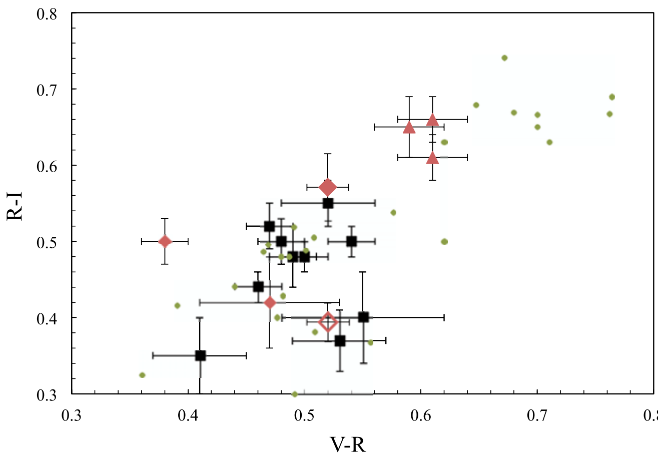

Figure 5. $R - I$ vs. $V - R$ for 2010 WG9 (large filled and unfilled red diamonds), other HiHq TNOs (medium-sized red diamonds), TNOs from the inner Oort Cloud (red triangles), Damocloids (black squares), and Centaurs (small green points, with error bars not shown to avoid crowding of the figure). The colors for 2010 WG9 are consistent with all of these populations, except perhaps the few observed inner-Oort-Cloud bodies.

(A color version of this figure is available in the online journal.)

surface composition, dominated by carbonaceous material with some fraction of polymerized organics. The presence or absence of surface water ice and/or volatile ices (e.g., methane, CO_2) cannot be ascertained from visual photometry alone. The object has the reddest spectral slope of the three known HiHq TNOs at V-band wavelengths (∼0.6 um), and it has either the reddest or the bluest slope at R-band wavelengths (∼0.7 um) depending on the rotational phase. It is interesting that the variation in $R - I$ covers the whole range represented by the Damocloids. If the variance in red color among the Damocloids correlates with retention of a primordial organic, then 2010 WG9 may represent a body with a partially preserved and partially eroded surface. Other possible explanations for the variation in color are patchy areas of volatile ices (as on Pluto), or the presence of a large crater that has exposed relatively neutral-colored sub-surface material (water ice, or un-irradiated carbonaceous material).

Recently, Kiss et al. (2013) report optical colors and thermal IR measurements of 2012 DR30, a borderline HiHq object with $a = 1109$ AU, $i = 78°$, $q = 14.54$ AU, and diameter 185 km. This body might have followed a migration route from the Oort Cloud like that of 2010 WG9, in which case it has since remained at distances beyond ∼15 AU from the Sun. But it is equally likely that the object followed a migration route typical of long-period comets, with previous close encounters with Jupiter or Saturn pulling the orbit out of the Oort Cloud. Hence, it may have experienced significant solar heating subsequent to its capture. The optical colors for 2012 DR30 are similar to 2010 WG9, except at blue wavelengths where the spectral slope is significantly flatter. On the basis of this feature and an absorption they observe in the z band, Kiss et al. suggest that 2012 DR30 could be a V-type asteroid from the main belt. This interpretation could not apply to 2010 WG9, owing to its significantly larger perihelion and color differences.

4.2. *Rotation*

The slow rotation period we measure for 2010 WG9 is extraordinary. Most known KBOs and asteroids have orbit periods of less than a day. Only a few dozen main-belt asteroids are known to have such very slow rotations (Masiero et al. 2009). Among these much smaller bodies, the slow rotation might be expected from the Yarkovsky effect (Pravec et al. 2005). But such slowing is not expected for ∼100 km diameter bodies at large distances from the Sun, such as 2010 WG9. Of the ∼100 TNOs and Centaurs with measured periods, the mean period is ∼7 hr and all but a few have periods <26 hr (Duffard et al. 2009; Benecchi & Sheppard 2013). The only known distant bodies with rotation periods much longer than one day are the synchronously locked binary objects Pluto/Charon and Sila/Nunam (Grundy et al. 2012). This suggests that 2010 WG9 may be a similar tidally evolved binary system.

Assuming 2010 WG9 is a system composed of two equal mass bodies on circular orbits about their center of mass, we can estimate their separation, Δ, based on an estimate of their combined mass, m. We start with the absolute V-band magnitude which we measure to be $H = H_R + V - R = 7.9{+}0.52 = 8.4$. Known TNOs with comparable absolute magnitudes have measured diameters of ∼100 km (Stansberry et al. 2008). If the binary consists of two bodies of equal albedo and size, then their individual diameters are $100/2^{1/2} \sim 70$ km. Scaling from Pluto's known mass (1.33×10^{22} kg) and diameter (2.4×10^3 km) and assuming a density of 1 gm cm^{-3} for the binary components (half the density of Pluto), we expect $m \sim 3.3 \times 10^{17}$ kg. Then using Kepler's law, we obtain $\Delta = 500$ km for an orbital period equal to the measured period, $P_L = 5.4955$ days, or $\Delta = 790$ km if the orbit period is twice the measured period, $2P_L = 10.991$ days. A known binary Centaur with comparable physical properties is the Typhon/Echidna system for which the component diameters are 112 and 56 km, the separation is ∼1300 km (Stansberry et al. 2012), and the orbital period is 18.97 days (Grundy et al. 2008). The binary Trojan Patroclus–Menoetius is also similar, composed of nearly equal sized bodies of ∼100 km diameter separated by 654 km with a synchronously locked rotation period of 4.29 days (Mueller et al. 2010). At the current distance of 18.8 AU for 2010 WG9, a separation of 790 km corresponds to an angular separation of $\sim 0\overset{''}{.}06$. Such separations are resolvable with the *Hubble Space Telescope* or large ground-based telescopes with adaptive optics (Grundy et al. 2011).

If 2010 WG9 is indeed a tidally locked binary system, then the color variation we see with rotational phase could relate to different surface properties for the facing and opposing hemispheres of the two bodies. For example, Stern (2009) proposes that impact ejecta from closely separated binaries would coat the facing hemispheres of tidally locked partners over the age of the solar system. This is especially relevant for bodies with small separation-to-diameter ratios. For 2010 WG9, this ratio might be ∼15, one of the smallest for any known binary system. Alternatively, the color variation might relate to the formation mechanism of the binary. For example, the surface of Haumea is known to have a dark red spot (Lacerda 2009, 2010; Fraser & Brown 2009). Though this spectroscopic feature has not been linked to any specific topological features on the surface of Haumea, its existence may relate to surface heterogeneity stemming from the collision that likely generated Haumea's satellite system (Leinhardt et al. 2010).

5. CONCLUSIONS

We have presented photometric observations of 2010 WG9 revealing a very slow rotation period and a large variation in color with rotational phase. While the nominal color we observe is not unusual for a distant body, the slow rotation is extreme, observed previously only for tidally locked binaries in the Kuiper Belt. The object also happens to follow a very high-inclination orbit, suggesting that it is a member of the Oort Cloud captured by close approach to Uranus or Neptune. Could the unique photometric properties relate to its peculiar orbit? The variation in color may relate to partial retention of primordial surface volatiles or a primordial crust of irradiated, organic material. Clearly, additional observations are required to determine whether 2010 WG9 is a binary system and to better measure the variation in color with orbital phase. The future discovery of additional HiHq TNOs will also better determine their range of photometric properties and the physical properties of their parent population.

This work was funded by NASA planetary astronomy award NNX10AB31G. M.E.S. is supported by an NSF Astronomy and Astrophysics Postdoctoral Fellowship (AST-1003258). We also thank the hard-working SMARTS queue managers and observers and the support staff at La Silla. A. Sommer is thanked for excellent proofing.

REFERENCES

Benecchi, S., & Sheppard, S. 2013, AJ, 145, 124
Brasser, R., Duncan, M., Levison, H. F., Schwamb, M. E., & Brown, M. E. 2012a, Icar, 217, 1
Brasser, R., Schwamb, M. E., Lykawka, P. S., & Gomes, R. S. 2012b, MNRAS, 420, 3396
Duffard, R., Ortiz, J. L., Thirouin, A., Santos-Sanz, P., & Morales, N. 2009, A&A, 505, 1283
Fernandez, J. A., & Brunini, A. 2000, Icar, 145, 580
Fraser, W., & Brown, M. E. 2009, ApJ, 695, 1
Gladman, B., Kavelaars, J., Petit, J.-M., et al. 2009, ApJ, 697, 91
Grundy, W., Benecchi, S. D., Rabinowitz, D. L., et al. 2012, Icar, 220, 74
Grundy, W., Noll, K. S., Nimmo, F., et al. 2011, Icar, 213, 678
Grundy, W., Noll, K. S., Virtanen, J., et al. 2008, Icar, 197, 260
Hainaut, O., Boehnhardt, H., & Protopapa, S. 2012, A&A, 546, 115
Henden, A., Levine, S., Terrell, D., Smith, T. C., & Welch, D. 2012, JAAVSO, 40, 430
Jewitt, D. 2005, AJ, 129, 530
Kiss, C., et al. 2013, A&A, in press
Lacerda, P. 2009, AJ, 137, 3404
Lacerda, P. 2010, in IAU Symp. 263, Icy Bodies of the Solar System, ed. J. A. Fernández et al. (Cambridge: Cambridge Univ. Press), 192
Leinhardt, Z., Marcus, R., & Stewart, S. 2010, ApJ, 714, 1789
Levison, H., Dones, L., & Duncanm, M. 2001, AJ, 121, 2253
Masiero, J., Jedicke, R., Durech, J., et al. 2009, Icar, 204, 145
Mueller, M., Marchis, F., Emery, J. P., et al. 2010, Icar, 205, 505
Pravec, P., Harris, A. W., Scheirich, P., et al. 2005, Icar, 173, 108
Rabinowitz, D., Barkume, K., Brown, M. E., et al. 2006, ApJ, 639, 1238
Rabinowitz, D., Schaefer, B., & Tourtellotte, S. 2007, AJ, 133, 26
Rabinowitz, D., Schwamb, M. E., Hadjiyksa, E., & Tourtellotte, S. 2012, AJ, 144, 140
Schaller, E., & Brown, M. 2007, ApJ, 659, 61
Sheppard, S. 2010, AJ, 139, 1394
Sheppard, S., Lacerda, P., & Ortiz, J. 2008, in The Solar System Beyond Neptune, ed. M. A. Barucci, H. Boehnhardt, D. P. Cruikshank, & A. Morbidelli (Tucson, AZ: Univ. Arizona Press), 129
Stansberry, J., Grundy, W., Brown, M., et al. 2008, in The Solar System Beyond Neptune, ed. M. A. Barucci et al. (Tucson, AZ: Univ. Arizona Press), 161
Stansberry, J., Grundy, W., Mueller, M., et al. 2012, Icar, 219, 676
Stern, S. A. 2009, Icar, 199, 571
Zacharias, N., Finch, C., Girard, T., et al. 2013, AJ, 145, 44